

Research on the halo in ^{31}Ne with complex momentum representation method

Ya-Juan Tian,¹ Quan Liu,^{1,*} Tai-Hua Heng,^{1,†} and Jian-You Guo^{1,‡}

¹*School of physics and materials science, Anhui University, Hefei 230601, P.R. China*

(Dated: October 20, 2018)

Halo is one of the most interesting phenomena in exotic nuclei especially for ^{31}Ne , which is deemed to be a halo nucleus formed by a p -wave resonance. However, the theoretical calculations don't suggest a p -wave resonance using the scattering phase shift approach or complex scaling method. Here, we apply the complex momentum representation method to explore resonances in ^{31}Ne . We have calculated the single-particle energies for bound and resonant states together with their evolutions with deformation. The results show that the p -wave resonances appear clearly in the complex momentum plane accompanied with the $p-f$ inversion in the single-particle levels. As it happens the $p-f$ inversion, the calculated energy, width, and occupation probabilities of major components in the level occupied by valence neutron support a p -wave halo for ^{31}Ne .

PACS numbers: 21.10.Gv, 21.10.Pc, 25.70.Ef, 24.30.-v

I. INTRODUCTION

Research on the nuclei far from the β -stability line, especially close to the neutron drip line, is a hot topic in nuclear physics. These nuclei with large ratio N/Z compared to their isotopes may have new features: the emergence of halo [1], the disappearance of traditional magic number and the generation of new magic number [2], and so on. One of the most interesting characteristics is the halo: one (or two) weakly-bound valence nucleon(s) spatially extend(s) far beyond the nuclear core by means of the quantum tunneling effect. This structure is ascribed to an occupation of the $l=0$ or $l=1$ orbit by valence nucleon [3]. The first confirmed halo structure appears in ^{11}Li , which is considered as two valence neutrons occupying the $2s_{1/2}$ orbit [4]. Afterwards, more halo structures such as s -wave halo and p -wave halo, two-body halo and three-body halo, etc. were explored and researched in experiments [5] and theories [6].

In these researches on halo nuclei, ^{31}Ne has received more attention since it is located in a mixing region of normal and intruder shell configurations. According to the shell model's scenarios, ^{31}Ne ground state should be a ^{30}Ne core in its 0^+ ground state with a $1f_{7/2}$ valence neutron. However, the calculations in Refs. [7, 8] favored this valence neutron populating in the $2p_{3/2}$ intruder orbit. The orbit with low one-neutron separation energy ($S_n \simeq 0.33$ MeV [9]) supports a halo structure. The one-neutron removal cross sections measured at RIKEN [10] suggested that ^{31}Ne is a halo nucleus. The data can be most easily interpreted as the ground state spin parity being $3/2^-$ rather than $7/2^-$. Further experiment [11] showed the interaction cross sections of ^{31}Ne are significantly greater than those of their neighboring nuclides, which cannot be explained by the single-particle shell

model under the assumption that the valence neutron occupies the $1f_{7/2}$ orbit.

In order to clarify the ground state spin-parity, some theoretical models were introduced for ^{31}Ne . In Ref. [12], the Glauber model was used to analyze the one-neutron removal cross sections. The result suggests a strong $2p_{3/2}$ configuration in the ^{31}Ne ground state. In the framework of the particle-rotor model, Urata *et al.* applied the Glauber theory to calculate the reaction cross sections, and found that the difference of the reaction cross sections between ^{30}Ne and ^{31}Ne is much larger for the configuration with $\beta_2 = 0.2$ than that with $\beta_2 = 0.55$, leading to a consistent description of one-neutron removal cross section with $\beta_2 = 0.2$ [13, 14]. Based on a quantitative analysis of the reaction cross sections of $^{28-32}\text{Ne}$ by ^{12}C at 240 MeV/nucleon using the double-folding model, Minomo *et al.* concluded that neutron-rich Ne isotopes are strongly deformed and ^{31}Ne has a halo structure with the spin parity $3/2^-$ [15, 16]. Using the density obtained by antisymmetrized molecular dynamics, the double folding model well reproduces the measured interaction cross sections of ^{31}Ne with the quadruple deformation $\beta_2 \sim 0.4$ [17].

In addition to the reaction cross section, the knowledge on the single-particle resonances is critical to understand the halo structure of exotic nuclei. In Ref. [18], the scattering phase shift approach was applied to explore the single-particle resonances in ^{31}Ne in a deformed mean field. The observed large Coulomb breakup cross section of ^{31}Ne can be interpreted in terms of p -wave neutron halo together with the deformed core ^{30}Ne . With the analytic continuation approach for resonances, ^{31}Ne is predicted to possess a p -orbit one-neutron halo structure based on the criteria of a large matter radius, low separation energy, and large population of a low- l orbit [19]. The halo structure of ^{31}Ne was also claimed from an occupation of the weakly bound level $1/2[330]$ by valence neutron in the complex scaling calculations [20].

All these are inclined to think that ^{31}Ne is a deformed halo nucleus with the spin parity $3/2^-$. However, we don't know that the $3/2^-$ comes from the $2p_{3/2}$ or $1f_{7/2}$

*E-mail: quanliu@ahu.edu.cn

†E-mail: hength@ahu.edu.cn

‡E-mail: jianyou@ahu.edu.cn

orbit and whether it happens the $p-f$ inversion in ^{31}Ne . Since the $2p_{3/2}$ and $1f_{7/2}$ orbits in ^{31}Ne have positive energy, it is necessary to treat the resonant states. The calculations in Ref. [18] exposed the $1f_{7/2}$ resonance, but the $2p_{3/2}$ resonance is missed. Although more resonant states are obtained in the complex scaling calculations [20], the $2p_{3/2}$ resonance has not been discovered. The reason may be that the $2p_{3/2}$ state corresponds to a broad resonance, while broad resonance is difficult to obtain in theory. Recently, we have developed a complex momentum representation (CMR) method for resonances [21, 22], which is effective for not only narrow resonances but also broad resonances with many advantages in comparison with some other methods [21, 23].

In the present paper we apply the complex momentum representation method to explore the resonant states in ^{31}Ne . The missed $2p_{3/2}$ resonance is obtained in accompanying with the $1f_{7/2}$ resonance. The $p-f$ inversion is exposed clearly in the single particle levels. Moreover, we have calculated the density distributions and the occupation probabilities of major components, which support a p -wave halo nucleus for ^{31}Ne . In the following, we express the theoretical formalism in Sec. II. In Sec. III, we present numerical details and results. A summary is collected in Sec. IV.

II. FORMALISM

To explore the resonances in ^{31}Ne , we first present the theoretical formalism of complex momentum representation method with the Hamiltonian as

$$H = T + V, \quad (1)$$

where T is the kinetic operator and V is the interaction potential. The kinetic energy operator $T = p^2/2m$ with the reduced mass m and momentum $\vec{p} = \hbar\vec{k}$ (\vec{k} is the wavevector). Following Ref. [24], the adopted interaction potential V consists of three parts

$$\begin{aligned} V_{\text{cent}}(r) &= V_0 f(r), \\ V_{\text{def}}(\vec{r}) &= -\beta_2 k(r) Y_{20}(\vartheta, \varphi), \\ V_{\text{sl}}(r) &= -4V_0 \Lambda^2 \frac{1}{r} \frac{df(r)}{dr} (\vec{s} \cdot \vec{l}), \end{aligned} \quad (2)$$

with

$$\begin{aligned} f(r) &= \frac{1}{1 + e^{\frac{r-R}{a}}}, \\ k(r) &= V_0 r \frac{df(r)}{dr}. \end{aligned}$$

Here, a , V_0 , and R represent respectively the diffuseness, depth, and range of the potential with $R = r_0 A^{1/3}$, where A is mass number of a nucleus and $r_0 = 1.27$ fm. Λ is the reduced Compton wavelength of nucleon. The solutions of Eq. (1) include the bound states, resonant states, and the continuum. The bound states can be obtained by the

conventional methods. In order to access the resonant states, the momentum representation is adopted with the Schrödinger equation as

$$\int d\vec{k}' \langle \vec{k} | H | \vec{k}' \rangle \psi(\vec{k}') = E \psi(\vec{k}), \quad (3)$$

where $\psi(\vec{k})$ is the momentum wavefunctions. For an axially deformed system, the parity π and the third component of total angular momentum m_j are good quantum numbers. Hence, we can expand the wavefunctions as

$$\psi(\vec{k}) = \psi_{m_j}(\vec{k}) = \sum_{l_j} f^{lj}(k) \phi_{l_j m_j}(\Omega_k), \quad (4)$$

where $f^{lj}(k)$ is the radial components of wavefunctions in momentum representation with the quantum numbers of the orbital angular momentum and total angular momentum l and j . The angular part of wavefunctions is represented as

$$\phi_{l_j m_j}(\Omega_k) = \sum_{m_s} \langle l m \frac{1}{2} m_s | j m_j \rangle Y_{lm}(\Omega_k) \chi_{m_s}, \quad (5)$$

where χ_{m_s} is the spin wavefunction with the third component of spin angular momentum m_s , and $Y_{lm}(\Omega_k)$ is the spherical harmonics in momentum space. Putting the wavefunctions (4) into the equation (3), the Schrödinger equation becomes

$$\begin{aligned} \frac{\hbar^2 k^2}{2M} f^{lj}(k) + \int k'^2 dk' V_s(l, j, k, k') f^{lj}(k') \\ - \beta_2 \sum_{l' j'} \int k'^2 dk' V_d(l, j, l', j', m_j, k, k') f^{l' j'}(k') \\ = E f^{lj}(k), \end{aligned} \quad (6)$$

with

$$V_s(l, j, k, k') = \frac{2}{\pi} \int r^2 dr [V_{\text{cent}}(r) + V_{\text{sl}}(r)] j_l(kr) j_l(k'r),$$

and

$$\begin{aligned} V_d(l, j, l', j', m_j, k, k') \\ = i^{3l+l'} \frac{2}{\pi} \int r^2 dr k(r) j_l(kr) j_{l'}(k'r) \\ \cdot \sum_{m_s} \langle l m | Y_{20}(\Omega_r) | l' m' \rangle \langle l m \frac{1}{2} m_s | j m_j \rangle \langle l' m' \frac{1}{2} m_s | j' m_j \rangle, \end{aligned}$$

where $j_l(kr)$ and $j_{l'}(k'r)$ are respectively the spherical bessel functions of order l and l' . It is difficult to solve the integral equation Eq. (6). For this reason, we transform the integral into a sum over a finite set of points k_a and dk with a set of weights w_a . And then, the integral equation becomes a matrix equation

$$\begin{aligned} \frac{\hbar^2 k_a^2}{2M} f^{lj}(k_a) + \sum_b w_b k_b^2 V_s(l, j, k_a, k_b) f^{lj}(k_b) \\ - \beta_2 \sum_{l' j'} \sum_b w_b k_b^2 V_d(l, j, l', j', m_j, k_a, k_b) f^{l' j'}(k_b) \\ = E f^{lj}(k_a). \end{aligned} \quad (7)$$

The Hamiltonian matrix in Eq. (7) is not symmetrical. For simplicity in computation, we symmetrize the Hamiltonian matrix by the transformation

$$f(k_a) = \mathbf{f}(k_a)/\sqrt{w_a k_a}. \quad (8)$$

Putting Eq. (8) into Eq. (7), we obtain a symmetric matrix equation in the momentum representation as

$$\begin{aligned} & \frac{\hbar^2 k_a^2}{2M} \mathbf{f}^{lj}(k_a) + \sum_b \sqrt{w_a w_b} k_a k_b V_s(l, j, k_a, k_b) \mathbf{f}^{lj}(k_b) \\ & - \beta_2 \sum_b \sum_{l'j'} \sqrt{w_a w_b} k_a k_b V_d(l, j, l', j', m_j, k_a, k_b) \mathbf{f}^{l'j'}(k_b) \\ & = E \mathbf{f}^{lj}(k_a). \end{aligned} \quad (9)$$

So far, to solve the Schrödinger equation becomes an eigensolution problem of the symmetric matrix. All the bound states and resonant states can be acquired simultaneously by diagonalizing the Hamiltonian in Eq. (9). The diagonalization of the Hamiltonian matrix in Eq. (9) can give us the energies and wavefunctions in the momentum space. To obtain the wavefunctions in the coordinate space, the following transformation is adopted

$$\psi(\vec{r}) = \psi_{m_j}(\vec{r}) = \frac{1}{(2\pi)^{3/2}} \int d\vec{k} e^{i\vec{k}\cdot\vec{r}} \psi_{m_j}(\vec{k}). \quad (10)$$

Assuming that the $\psi_{m_j}(\vec{r})$ holds the form

$$\psi_{m_j}(\vec{r}) = \sum_{lj} f^{lj}(r) \phi_{ljm_j}(\Omega_r), \quad (11)$$

we can obtain the radial part of wavefunctions

$$f^{lj}(r) = i^l \sqrt{\frac{2}{\pi}} \sum_{a=1}^N \sqrt{w_a} k_a j_l(k_a r) \mathbf{f}^{lj}(k_a), \quad (12)$$

and the radial density distributions

$$\rho_{m_j}(r) = \sum_{lj} f^{lj*}(r) f^{lj}(r). \quad (13)$$

III. NUMERICAL DETAILS AND RESULTS

With the formalism represented above, we explore the single-particle resonances in ^{31}Ne in order to clarify the physical mechanism of ^{31}Ne halo. Before starting the researches, we introduce numerical details. In the present calculations, the coupled-channel method is adopted to solve the equation of motion describing deformed nuclei, and the wavefunctions are expanded with different channels labeled as lj . The sum over lj in Eq. (4) is restricted to a limited range $N_c = 8$. In Eq. (6), the momentum integration from zero to infinite is truncated to a large enough $k_{max} = 4.0 \text{ fm}^{-1}$, and replaced by a sum using the Gauss-Legendre quadrature with a finite grid number $N_l = 120$. The choice of these parameter values is enough to ensure the required precision.

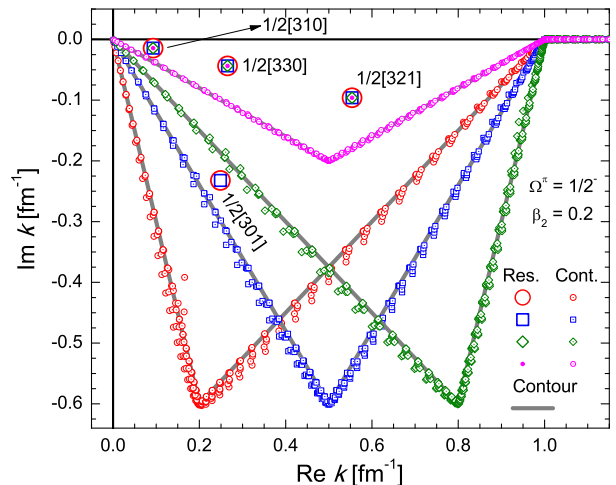


FIG. 1: (Color online) Single-particle spectra for the states $\Omega^\pi = 1/2^-$ with $\beta_2 = 0.2$ in complex momentum plane, where the red open circles, blue hollow squares, green hollow rhombus, and magenta points represent the resonant states in four different contours, respectively. The other is the continuum following the contours in grey solid line.

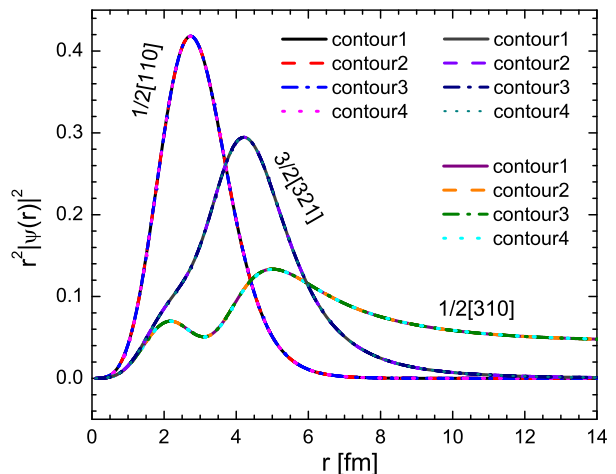


FIG. 2: (Color online) Radial density distributions as a function of the coordinate r for the single-particle states $1/2[110]$ and $1/2[310]$ with $\beta_2 = 0.2$ and $3/2[321]$ with $\beta_2 = 0.5$. The left four lines belong to $1/2[110]$, the upper four lines on the right belong to $3/2[321]$, and those in the lower belong to $1/2[310]$. The four contours are the same as those in Fig. 1.

With these parameters designed, we check the validity and applicability of present calculations. The numerical results for the states $\Omega^\pi = 1/2^-$ with the deformation $\beta_2 = 0.2$ are shown in Fig. 1, where the four different contours are adopted in the momentum integration. The resonant states are completely independent on the contours. With the contour becomes deeper from the magenta color to the blue color and/or the contour from left (red color) to right (green color), the resonant states always stay at their original locations in the complex momentum plane. The resonant state $1/2[301]$ is located

outside the magenta and green contours. Hence, it is necessary to select a large enough contour to expose all the resonant states concerned.

In addition to the single particle energies, the wavefunctions are also independent of contours. In Fig. 2, we have plotted the radial density distributions as a function of the coordinate r for the single-particle states $1/2[110]$, $1/2[310]$, and $3/2[321]$. The state $1/2[110]$ is deeply bound over the range of deformation under consideration. The state $1/2[310]$ locates at a resonant orbit with $\beta_2 = 0.2$. The state $3/2[321]$ is weakly bound in the position of $\beta_2 = 0.5$. Whether the bound state, the resonant state, or the weakly bound state, the calculated density distributions with the four different contours completely coincide together, which indicates the wavefunctions are independent of contours. Compared with the bound state $1/2[110]$, the radial density distributions for the resonant state $1/2[310]$ and the weakly bound state $3/2[321]$ spatially extend in a larger range, which indicates that a halo may be formed if a nucleon populates in the orbits.

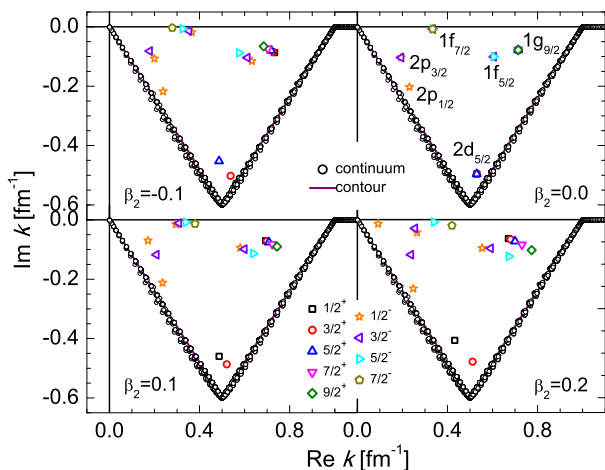


FIG. 3: (Color online) Single-particle spectra of ^{31}Ne for the states $\Omega^\pi = 1/2^\pm, 3/2^\pm, \dots, 9/2^\pm$ in several different deformations. The black open circles and purple solid line represent respectively the continuum and contour of momentum integration, and the other represent the resonant states.

As the resonant states are independent of the contours, we can select a large enough contour to expose all the resonant states concerned. Using the triangle contour with the four points $k = 0 \text{ fm}^{-1}$, $k = 0.5 - i0.6 \text{ fm}^{-1}$, $k = 1.0 \text{ fm}^{-1}$, and $k = 4.0 \text{ fm}^{-1}$, these resonant states concerned are obtained over the range of deformation under consideration. In Fig. 3, we have presented the solutions of Eq. (9) for the states $\Omega^\pi = 1/2^\pm, 3/2^\pm, \dots, 9/2^\pm$ in several different deformations. It is noticed that the positions of the resonant states in complex momentum plane depend on the deformation β_2 . When the spherical symmetry is broken ($\beta_2 \neq 0$), the states $2p_{3/2}$, $1f_{5/2}$, $1f_{7/2}$ and $1g_{9/2}$ are split into two, three, four, and five resonant states, respectively. Similarly, the state $2d_{5/2}$ is split into three resonant states. When $\beta_2 = -0.1$, only

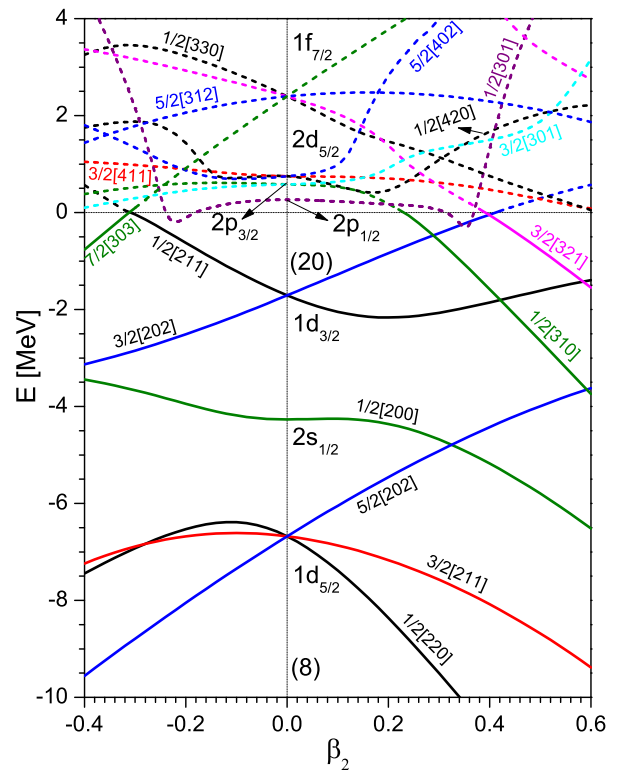


FIG. 4: (Color online) Neutron single-particle levels as a function of quadrupole deformation β_2 . The bound levels and resonant levels are marked by the solid line and dashed line, respectively.

the $5/2^+$ and $3/2^+$ states emerge in the complex momentum plane, while the $1/2^+$ state is beyond the range of contour. When $\beta_2 = 0.1$ and $\beta_2 = 0.2$, only the $1/2^+$ and $3/2^+$ states appear in the complex momentum plane, while the $5/2^+$ state lies outside of the contour. These show that some resonances may move into the contour and some other resonances may be removed from the contour with the change of deformation.

Making clear the dependence of the resonance on deformation, let's explore the mechanism of deformation halo in ^{31}Ne . The calculated single-particle energies for all the bound and resonant states concerned are shown in Fig. 4, where the bound (resonant) levels are marked by the solid (dashed) line with the Nilsson labels on the line. The corresponding spherical labels are marked in the position $\beta_2 = 0.0$. From Fig. 4, it can be seen that the bound levels are the fully same as those in Refs. [18, 20]. For the resonant levels, only those with the spherical labels $1f_{7/2}$ are obtained in the scattering phase shift calculations [18]. Although the more resonant levels including those with the spherical labels $1f_{5/2}$, $1f_{7/2}$, and $1g_{9/2}$ are obtained in the complex scaled calculations [20], these resonant levels with the spherical labels $2p_{3/2}$, $2p_{1/2}$, and $2d_{5/2}$ are still missed. Since the halo is mainly attributed to an occupation of the orbit with lower angular momentum and separation energy by valance nucleon, these

resonant levels with the spherical labels $2p_{3/2}$, $2p_{1/2}$, and $2d_{5/2}$ are more attractive. Unfortunately, these resonant levels have not been obtained in the scattering phase shift calculations and the complex scaling calculations. Furthermore, the levels $1/2[310]$ and $1/2[330]$ obtained in the scattering phase shift is questionable. With the decrease of deformation from $\beta_2 = 0.6$ to $\beta_2 = 0.0$, the $1/2[310]$ level evolves from a bound state to a resonant state. At $\beta_2 = 0.0$, the $1/2[310]$ level degenerates the $2p_{3/2}$ level rather than the $1f_{7/2}$ level. Over the range of deformation, the $1/2[330]$ level is always located in the resonant region, while it is incorrectly connected to the level $1/2[310]$ in Ref. [18]. With these resonant levels in the spherical labels $2p_{3/2}$, $2p_{1/2}$, and $2d_{5/2}$ obtained, an inverted ordering of $p-f$ orbits is discovered in comparison with the usual shell model prediction. As it happens the $p-f$ inversion, the 21st neutron in ^{31}Ne can occupy a p -orbit or that with major p -component, which is the cause of the halo formed in ^{31}Ne . Assuming that ^{31}Ne is a prolate nucleus, the 21st neutron may occupy the levels $1/2[301]$, $1/2[310]$, $3/2[202]$, $3/2[321]$, and $1/2[211]$ in the intervals of $0.0 \leq \beta_2 \leq 0.20$, $0.20 \leq \beta_2 \leq 0.29$, $0.29 \leq \beta_2 \leq 0.40$, $0.40 \leq \beta_2 \leq 0.59$, and $\beta_2 \geq 0.59$, respectively. Which orbit is the most appropriate for ^{31}Ne ? The state $1/2[301]$ locates in the resonant level. If a nucleon occupies the level, its density distribution can spatially extend far beyond the nuclear core. However, there exists a large energy gap in the interval of $0.0 \leq \beta_2 \leq 0.20$, which increases the difficulty of nucleon occupying the orbit. According to the claim in Ref. [3], the halo structure is ascribed to an occupation of the $l = 0$ or $l = 1$ orbit by valence nucleon with lower separation energy. From this view, the appropriate orbit may be $1/2[310]$ in the interval of $0.20 \leq \beta_2 \leq 0.29$ or $3/2[321]$ in the interval $0.40 \leq \beta_2 \leq 0.59$. The result agrees with the calculations in Ref. [13, 14], where the ground state of ^{31}Ne is predicted with the configurations of $I^\pi = 3/2^-$ at $\beta_2 = 0.2$ or 0.55 . In Ref. [15, 16], Minomo *et al.* concluded that neutron-rich Ne isotopes are strongly deformed and ^{31}Ne has a halo structure with the spin parity $3/2^-$. The similar conclusion is obtained in Ref. [17] for ^{31}Ne with the deformation $\beta_2 \sim 0.4$. In addition, an appropriate configuration $3/2[321]$ is predicted with the deformation in the interval $0.40 < \beta_2 < 0.59$ for the ground state of ^{31}Ne in Ref. [18]. These conclusions are in agreement with our calculations with the inclination of the orbit $3/2[321]$ in large deformation.

In order to identify the most likely orbit in favor of halo in ^{31}Ne , we compare the occupation probabilities of major components in the levels $1/2[310]$ and $3/2[321]$. The calculated occupation probabilities of major components as a function of deformation β_2 are plotted in Fig. 5 for the level $1/2[310]$. Over the range of deformation, the occupation probabilities of the four components $p_{3/2}$, $f_{7/2}$, $p_{1/2}$, and $f_{5/2}$ are observable, while the other components are negligible. At $\beta_2 = 0.0$, the level $1/2[310]$ degenerates the spherical configuration $2p_{3/2}$, which supports the result from the level $1/2[310]$ in Fig. 4. With the increase

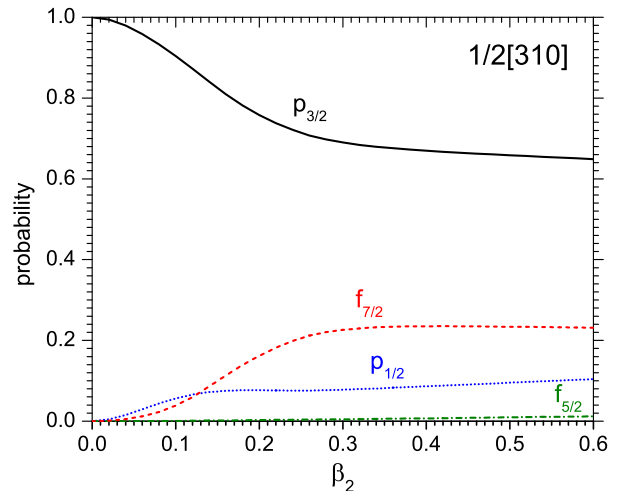


FIG. 5: (Color online) Calculated occupation probabilities of major components in the $1/2[310]$ level, where the black solid line, red dashed line, blue dotted line, and green dash-dotted line represent the $p_{3/2}$, $f_{7/2}$, $p_{1/2}$, and $f_{5/2}$ components, respectively.

of deformation, the occupation probability of $p_{3/2}$ decreases, while the occupation probabilities of $f_{7/2}$, $p_{1/2}$, and $f_{5/2}$ increase. Even so, the wavefunction of the level $1/2[310]$ is mostly constituted by the $p_{3/2}$ configuration. Within the range of deformation, the occupation probability of $p_{3/2}$ is over 64%, which indicates that the level $1/2[310]$ satisfies the condition of halo formation and the halo in ^{31}Ne may come from an occupation of the orbit $1/2[310]$ by valence neutron.

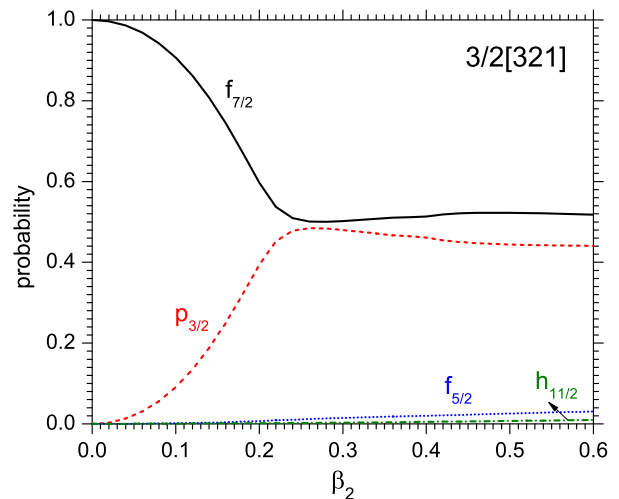


FIG. 6: (Color online) Calculated occupation probabilities of major components in the $3/2[321]$ level, where the black solid line, red dashed line, blue dotted line, and green dash-dotted line represent the $f_{7/2}$, $p_{3/2}$, $f_{5/2}$, and $h_{11/2}$ components, respectively.

For comparison, we have also plotted the occupation

probabilities of major components in the wavefunction of the level $3/2[321]$ as a function of β_2 in Fig. 6. Similar to the level $1/2[310]$, only the four components $f_{7/2}$, $p_{3/2}$, $f_{5/2}$, and $h_{11/2}$ are observable, while the other components are insignificant. At $\beta_2 = 0$, the level $3/2[321]$ degenerates the spherical configuration $1f_{7/2}$, which agrees the case in Fig. 4. With the increase of deformation from $\beta_2 = 0$ to $\beta_2 = 0.26$, the occupation probability of $f_{7/2}$ decreases, while the occupation probabilities of $p_{3/2}$, $f_{5/2}$, and $h_{11/2}$ increase. Further increasing the deformation, the occupation probabilities of $f_{7/2}$ and $p_{3/2}$ do almost unchange and the wavefunction of the level $3/2[321]$ is mostly constituted by the $f_{7/2}$ and $p_{3/2}$ configurations. As the occupation probability of $p_{3/2}$ in the wavefunction of the level $3/2[321]$ is over 44%, the level $3/2[321]$ also supports the formation of halo. However, the energy gap between the levels $3/2[321]$ and $1/2[211]$ is considerably large in the interval $0.40 \leq \beta_2 \leq 0.50$. If nuclear deformation is larger than $\beta_2 = 0.50$, the energy gap between the levels $3/2[321]$ and $1/2[211]$ becomes small, the halo in ^{31}Ne is most likely derived from an occupation of the orbit $3/2[321]$ by a valance neutron. Nevertheless, the large contamination of f -wave in $3/2[321]$ implies that the core excited component $^{30}\text{Ne}(2^+) \otimes f_{7/2}$ is non-negligible, if the ground state is $3/2^-$.

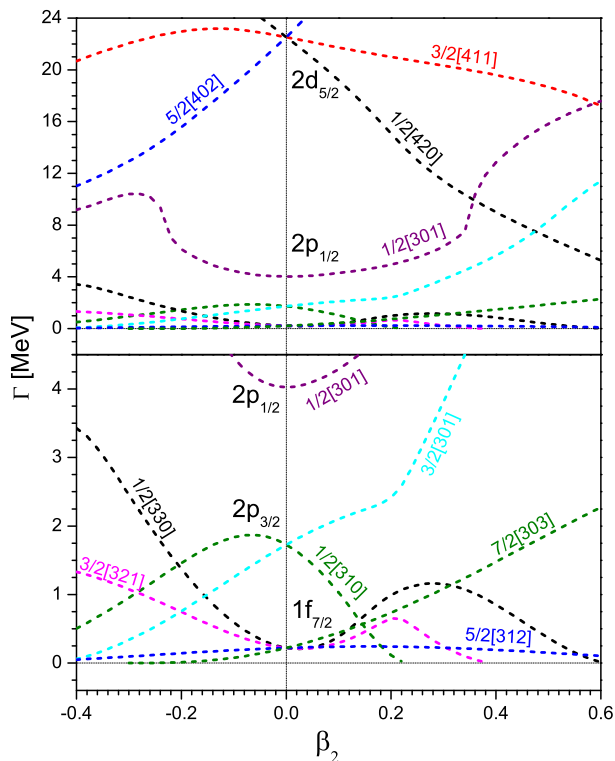


FIG. 7: (Color online) The same as Fig. 4, but for the width of resonant states.

With the knowledge on the energy levels (positions) of resonant states, let's figure out the widths of resonant states. The widths as a function of deformation β_2 is drawn in the upper panel in Fig. 7 for all the reso-

nant states concerned. The lower panel in Fig. 7 is a close-up of the widths for these resonant states near zero energy surface. For simplicity in comparison, the marks of the widths in Fig. 7 are the fully same as those of the levels shown in Fig. 4. Similar to the levels, there exists the shell structure in the widths. It is different where appears the energy gap. For the levels, a large energy gap appears between the states $1f_{7/2}$ and $2d_{5/2}$ at $\beta_2 = 0.0$. However for the widths, an unexpected gap appears between the states $2d_{5/2}$ and $2p_{1/2}$ at $\beta_2 = 0.0$. In addition, the order of the widths is different from that of the levels. The resonant level $2d_{5/2}$ lies between the levels $1f_{7/2}$ and $2p_{3/2}$, while the corresponding width is located above them. Due to the lower centrifugal barrier, the width of a p -state is usually greater than that of a f -state, which can be seen in the lower panel of Fig. 7. With the increase of deformation, the level $2p_{3/2}$ is split into two levels $1/2[310]$ and $3/2[301]$. The resonant state $1/2[310]$ becomes more stable with the increase of deformation from $\beta_2 = 0.0$, while the states $3/2[301]$ and $1/2[301]$ become more unstable. Hence, it is relatively easy to form halo in the resonant state $1/2[310]$ in ^{31}Ne . Similar phenomena also emerge in the f -state. With the increase of deformation, the level $1f_{7/2}$ is split into four levels $1/2[330]$, $3/2[321]$, $5/2[312]$, and $7/2[303]$. The resonant state $3/2[321]$ becomes more unstable with the increase of deformation from $\beta_2 = 0.0$ to $\beta_2 = 0.2$. Further increasing deformation, the resonant state $3/2[321]$ becomes more stable, which implies that the state $3/2[321]$ also supports the formation of halo in ^{31}Ne in the region of large deformation. The conclusion is in agreement with that obtained in terms of the single-particle levels. All these show that ^{31}Ne is a halo nucleus formed by $p_{3/2}$ configuration.

In order to provide the possible observables for experiment, in Fig. 8 we have plotted the radial-momentum probability distributions for the state $1/2[310]$ with $\beta_2 = 0.25$ and $3/2[321]$ with $\beta_2 = 0.5$. The remarkable differences in the position and height of peak and the range of radial-momentum probability distributions can be identified by the knock-out reaction, which is helpful to distinguish the two orbits.

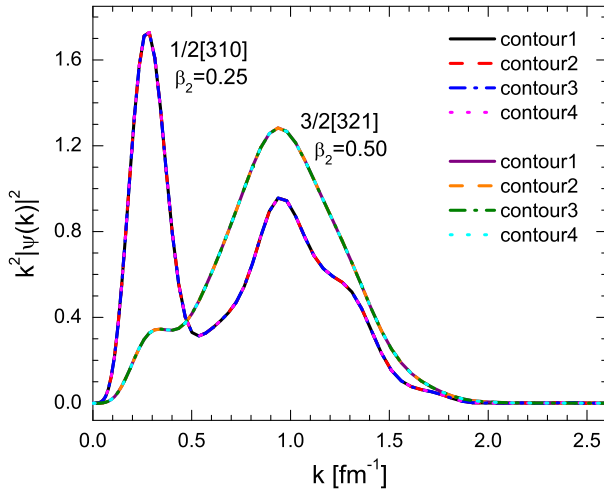


FIG. 8: (Color online) Radial-momentum probability distributions for the state $1/2[310]$ with $\beta_2 = 0.25$ and $3/2[321]$ with $\beta_2 = 0.5$, where the upper and lower four lines belong to $1/2[310]$ and $3/2[321]$, respectively.

IV. SUMMARY

In summary, the complex momentum representation method is used to explore the physical mechanism of deformed halo in ^{31}Ne with the theoretical formalism presented. The Schrödinger equation describing deformed nuclei is processed into a set of coupled differential equations by the coupled-channel method. This set of coupled differential equations is solved using the complex momentum representation technique, which makes the solutions of the Schrödinger equation become the diagonalization of a matrix, and the bound and resonant states

are treated on the equaling footing. The dependence of the calculations on the unphysical parameters is checked, satisfactory result is obtained.

The single-particle resonant states in ^{31}Ne are explored. Not only the narrow resonance $1f_{7/2}$ but also the broad resonances $2p_{3/2}$, $2p_{1/2}$, and $2d_{5/2}$, which are missed in the scattering phase shift and the complex scaling calculations, are obtained. As these broad resonances come into sight, the $p-f$ inversion is seen clearly in the single-particle levels. As a result, the 21st neutron in ^{31}Ne can occupy a p -orbit or that with major p -component, which is the cause of the halo formed in ^{31}Ne . From the position and energy gap, it can be judged that two appropriate Nilsson orbits are $1/2[310]$ in the interval of $0.20 \leq \beta_2 \leq 0.29$ and $3/2[321]$ in the interval $0.40 \leq \beta_2 \leq 0.59$. Over the range of deformation, the wavefunction of the level $1/2[310]$ is mainly constituted by the $p_{3/2}$ configuration, which supports the formation of halo. When $\beta_2 \geq 0.40$, the occupation probability of $p_{3/2}$ in the state $3/2[321]$ is over 44%, which also supports the formation of halo. All these show that ^{31}Ne is a halo nucleus formed by the $p_{3/2}$ configuration. This conclusion is also supported by the calculated widths.

Acknowledgments

This work was partly supported by the national natural science foundation of China (11575002, 11175001, and 11305002); the program for new century excellent talents in university of China (NCET-05-0558); the foundation of academic and technical leaders in Anhui province (J05010247), and the Doctoral Scientific Research Startup Fund of Anhui University (J01001319-J10113190082).

-
- [1] I. Tanihata, H. Hamagaki and O. Hashimoto, *et al.*, *Phys. Rev. Lett.* **55**, 2676 (1985).
 - [2] A. Ozawa, T. Kobayashi, T. Suzuki, K. Yoshida, and I. Tanihata, *Phys. Rev. Lett.* **84**, 5493 (2000).
 - [3] H. Sagawa, *Phys. Lett. B* **286**, 7 (1992).
 - [4] J. Meng and P. Ring, *Phys. Rev. Lett.* **77**, 3963 (1996).
 - [5] I. Tanihata, H. Savajols, and R. Kanungo, *Prog. Part. Nucl. Phys.* **68**, 215 (2013).
 - [6] J. Meng and S. G. Zhou, *J. Phys. G: Nucl. Part. Phys.* **42**, 093101 (2015).
 - [7] A. Poves and J. Retamosa, *Nucl. Phys. A* **571**, 221 (1994).
 - [8] P. Descouvemont, *Nucl. Phys. A* **655**, 440 (1999).
 - [9] G. Audi, A. H. Wapstra, and C. Thibault, *Nucl. Phys. A* **729**, 337 (2003).
 - [10] T. Nakamura *et al.*, *Phys. Rev. Lett.* **103**, 262501 (2009).
 - [11] M. Takechi *et al.*, *Phys. Lett. B* **707**, 357 (2012).
 - [12] W. Horiuchi, Y. Suzuki, P. Capel, and D. Baye, *Phys. Rev. C* **81**, 024606 (2010).
 - [13] Y. Urata, K. Hagino, and H. Sagawa, *Phys. Rev. C* **83**, 041303(R) (2011).
 - [14] Y. Urata, K. Hagino, and H. Sagawa, *Phys. Rev. C* **86**, 044613 (2012).
 - [15] K. Minomo, T. Sumi, M. Kimura, K. Ogata, Y. R. Shimizu, and M. Yahiro, *Phys. Rev. C* **84**, 034602 (2011).
 - [16] K. Minomo, T. Sumi, M. Kimura, K. Ogata, Y. R. Shimizu, and M. Yahiro, *Phys. Rev. Lett.* **108**, 052503 (2012).
 - [17] T. Sumi *et al.*, *Phys. Rev. C* **85**, 064613 (2012).
 - [18] I. Hamamoto, *Phys. Rev. C* **81**, 021304(R) (2010).
 - [19] S. S. Zhang, M. S. Smith, Z. S. Kang, and J. Zhao, *Phys. Lett. B* **730**, 30 (2014).
 - [20] Q. Liu, J. Y. Guo, Z. M. Niu, and S. W. Chen, *Phys. Rev. C* **86**, 054312 (2012).
 - [21] N. Li, M. Shi, J. Y. Guo, Z. M. Niu, H. Z. Liang, *Phys. Rev. Lett.* **117**, 062502 (2016).
 - [22] Z. Fang, M. Shi, J. Y. Guo, Z. M. Niu, H. Z. Liang, and S. S. Zhang, *Phys. Rev. C* **95**, 024311 (2017).
 - [23] Y. J. Tian, T. H. Heng, Z. M. Niu, Q. Liu, J. Y. Guo, *Chin. Phys. C* **41**, 044104 (2017).
 - [24] I. Hamamoto, *Phys. Rev. C* **72**, 024301 (2005).